



Contents lists available at ScienceDirect

NeuroImage

journal homepage: www.elsevier.com/locate/neuroimage

Combining images and anatomical knowledge to improve automated vein segmentation in MRI



Phillip G.D. Ward^{a,b,c,d,*}, Nicholas J. Ferris^{a,e}, Parnesh Raniga^f, David L. Dowe^b,
Amanda C.L. Ng^g, David G. Barnes^h, Gary F. Egan^{a,c,d}

^a Monash Biomedical Imaging, Monash University, Clayton, VIC, Australia

^b Faculty of Information Technology, Monash University, Clayton, VIC, Australia

^c ARC Centre of Excellence for Integrative Brain Function, Melbourne, VIC, Australia

^d Monash Institute of Cognitive and Clinical Neurosciences, Monash University, Clayton, VIC, Australia

^e Monash Imaging, Monash Health, Clayton, VIC, Australia

^f The Australian eHealth Research Centre, CSIRO Health and Biosecurity, Herston, QLD, Australia

^g Department of Anatomy and Neuroscience, The University of Melbourne, Melbourne, VIC, Australia

^h Monash eResearch Centre, Monash University, Clayton, VIC, Australia

ARTICLE INFO

Keywords:

MRI
QSM
SWI
Vein atlas
Vein segmentation
Cerebral vasculature

ABSTRACT

Purpose: To improve the accuracy of automated vein segmentation by combining susceptibility-weighted images (SWI), quantitative susceptibility maps (QSM), and a vein atlas to produce a resultant image called a composite vein image (CV image).

Method: An atlas was constructed in common space from manually traced MRI images from ten volunteers. The composite vein image was derived for each subject as a weighted sum of three inputs; an SWI image, a QSM image and the vein atlas. The weights for each input and each anatomical location, called template priors, were derived by assessing the accuracy of each input over an independent data set. The accuracy of vein segmentations derived automatically from each of the CV image, SWI, and QSM image sets was assessed by comparison with manual tracings. Three different automated vein segmentation techniques were used, and ten performance metrics evaluated.

Results: Vein segmentations using the CV image were comprehensively better than those derived from SWI or QSM images (mean Cohen's $d = 1.1$). Sixty permutations of performance metric, benchmark image, and automated segmentation technique were evaluated. Vein identification improvements that were both large and significant (Cohen's $d > 0.80$, $p < 0.05$) were found in 77% of the permutations, compared to no improvement in 5%.

Conclusion: The accuracy of automated vein segmentations derived from the composite vein image was overwhelmingly superior to segmentations derived from SWI or QSM alone.

Introduction

Mapping cerebral veins using magnetic resonance (MR) images has until recently been technically challenging. Cerebral venograms are increasingly important for advancing our knowledge of cerebral vascularisation, oxygenation, metabolism, and studies of cerebrovascular topology. The use of venograms in clinical research applications is growing rapidly, including for quantifying oxygen saturation (Fan et al., 2014), measuring the metabolic rate of oxygen consumption (Rodgers et al., 2016), analyzing possible fMRI confounders (Vigneau-Roy et al., 2014), and planning neurosurgery (Grabner et al., 2017).

Traditional vein imaging techniques require invasive contrast agents, have potential arterial confounds, and are limited to the large vessels, due to the reduced volume and flow of smaller cerebrovasculature segments. However, magnetic susceptibility provides an intrinsic contrast mechanism that is exquisitely sensitive to the presence of iron, particularly deoxygenated iron-rich haemoglobin proteins within red blood cells, making susceptibility techniques very useful for imaging small as well as large veins. The magnetic susceptibility of blood is modulated by oxygen (Pauling and Coryell, 1936), which facilitates the separation of arteries and veins, whilst providing a mechanism to quantify oxygen saturation (Fan et al., 2014).

* Corresponding author. Monash Biomedical Imaging, Monash University, Clayton, VIC, Australia.

E-mail address: phillipgdward@gmail.com (P.G.D. Ward).

Susceptibility-weighted imaging (SWI) and quantitative susceptibility mapping (QSM) are MR techniques based on magnetic susceptibility that provide a non-invasive method of imaging the cerebral veins. QSM and SWI derive contrast from gradient-recalled echo (GRE) phase information and have been applied to stroke, multiple sclerosis, cerebrovascular disease, and examined in clinical and preclinical studies (Betts et al., 2016; Deistung et al., 2016; Fan et al., 2015; Fujima et al., 2011; Goodwin et al., 2015; Jain et al., 2010; Li et al., 2013; Liu and Li, 2016; Rodgers et al., 2013; Santhosh et al., 2009). The way in which SWI and QSM process the phase information is very different.

SWI multiplies a non-linear mapping of high-pass filtered GRE phase with the GRE magnitude image, compounding the effects of signal cancellation from incoherent signals within each voxel and phase accumulation due to local sources of magnetic susceptibility (Haacke et al., 2004). Non-local sources are also included, such as the extravascular phase information, resulting in the magnification of small veins. The presentation of non-local sources, and non-linear mapping, generates a non-quantitative image best suited to radiological interpretation.

QSM estimates the magnetic susceptibility distribution directly by inverting the magnetic field information captured in the phase image (Marques and Bowtell, 2005; Salomir et al., 2003). Mathematically, QSM involves a linear system inversion that is ill-posed and requires regularization or fitting (Li et al., 2015; Liu et al., 2017; Wang and Liu, 2015; Wharton et al., 2010). QSM has the benefits of being quantitative and is designed to resolve extravascular field effects, leaving only local sources of magnetic susceptibility contrast.

The differing approaches (QSM and SWI) have unique image contrasts, and each have their own vein-like confounders. SWI images, for instance, do not distinguish between signal cancellation due to venous blood, and low concentrations of free protons (Haacke et al., 2004). The lack of distinction is problematic when analyzing veins which reside near non-vein low signal structures, such as in the vicinity of the tentorium and in the interhemispheric fissure (due to the falx cerebri). Both SWI and QSM also suffer different artefacts, such as cruciform artefacts in QSM images. Additionally, vein contrast in both SWI and QSM is reduced by iron depositions. The high amount of iron, for instance in the basal ganglia, can impair venous segmentation.

As neither QSM nor SWI isolate blood signal intrinsically, unlike spin-labelling or contrast agent-based techniques, venous voxels within the brain must be identified before the veins can be analysed. The process of identifying venous voxels in the brain, or segmentation, produces a vein mask that can then be used to extract the vein signal from an image, or examined directly for topographic analysis. In this work, the term segmentation is used as a noun to refer to a binary mask that labels each voxel as vein or non-vein.

A number of algorithms for automatic segmentation of blood vessels in the body have been proposed, including shape-driven, intensity-driven and hybrid approaches (Lesage et al., 2009). A common approach in the analysis of SWI and QSM data is to employ a preliminary filtering step, such as Hessian-based filtering (Frangi et al., 1998), before applying a simple threshold classification method (Vigneau-Roy et al., 2014). Hessian-based filtering and thresholding has been used to construct a vein-atlas to study multiple-sclerosis (Grabner et al., 2014). These filtering techniques have also been applied to build vascular network models using both QSM (Kociński et al., 2017) and time-of-flight images (Hsu et al., 2017). Recent work has combined Hessian-based filtering into a segmentation framework with diffusion techniques to overcome noise and low vein visibility (Bazin et al., 2016; Manniesing et al., 2006). Statistical modeling of spatial relations has also been proposed to improve continuity and smoothness in vein segmentation (Bériault et al., 2014; Ward et al., 2017b).

The previously mentioned work focused upon SWI (Bériault et al., 2014; Vigneau-Roy et al., 2014) or QSM (Bazin et al., 2016; Kociński et al., 2017; Ward et al., 2017b), and did not attempt to extract information from both images. Methods have been proposed that merge SWI with QSM (Ward et al., 2015), SWI with R2* maps (Monti et al., 2015),

and QSM with both SWI and R2* (Deistung et al., 2013). These approaches were globally homogeneous, i.e., they combined voxel intensities without consideration for anatomical location. As SWI and QSM have differing image contrasts, and artefacts that are specific to anatomy, it is possible that an improved segmentation could be achieved if the method for combining the two images was sensitive to spatial location.

Prior anatomical knowledge has recently been incorporated into a vein segmentation technique to reduce false positives in specific brain regions (Bériault et al., 2015). However, this approach was limited to specific deep-brain regions (particularly the basal ganglia), it did not directly address boundaries between tissue types and neural structures, and it was hand-tuned.

There are two anatomical factors that contribute to vein segmentation accuracy. The first is vein anatomy, i.e., expected vein occurrence, size and shape at an anatomical location. The second is image contrast, i.e., expected tissue signal relative to vein signal, which is specific to SWI and QSM. In this study, these two factors are exploited to improve cerebrovenous contrast and subsequent vein segmentation accuracy. We propose a vein identification and segmentation method that is based on a locally varying combination of SWI and QSM contrast which is informed by known vein anatomy in specific neuroanatomical structures. The proposed method derives a single composite vein image (CV image) that incorporates the strengths of SWI and QSM, with the anatomical knowledge of a vein atlas.

The CV image is generated from three input images (SWI, QSM and atlas) that are combined using a weighted-sum. The weights are derived from template priors that capture the location-specific venous contrast of the three input images throughout the brain. Separate vein atlases and template priors were calculated for each subject within the study from an independent sample of the cohort to ensure data independence. Future applications of the technique would use a single template prior and atlas calculated from the entire cohort. The CV image was compared to SWI and QSM images for the purpose of vein segmentation using automated techniques. Segmented CV images were compared with segmented SWI and QSM images using a broad array of accuracy measures and three automated segmentation techniques.

Methods

All procedures were reviewed and approved by the local ethics committee. Informed consent was obtained from all volunteers. The code and data used in this study have been made available to the public using GitHub and figshare respectively (<https://doi.org/10.4225/03/57B6AB25DDBDC>) (Ward, 2017a; Ward et al., 2017c).

Data acquisition

Ten healthy volunteers were scanned using a 3T Siemens Skyra with a 32-channel head and neck coil (6 females, mean age 56.2 years, standard deviation 25.2). The protocol was a single echo, flow-compensated, gradient-recalled echo (GRE) sequence (orientation = axial, TE = 20 ms, TR = 30 ms, flip angle = 15°, voxel = 0.9 × 0.9 × 1.8 mm anisotropic, matrix 256 × 232 × 72). Four of the subjects were acquired with a smaller voxel size (voxel = 0.9 mm isotropic, matrix = 256 × 232 × 160). A T1-Weighted MPRAGE scan was also acquired and used for registration purposes (TE = 2 ms, TR = 2300 ms, TI = 900 ms, voxel = 1.0 mm isotropic, matrix = 240 × 256 × 192, flip angle = 9°).

T1-weighted images were non-linearly registered to MNI152 space (Montreal Neurological Institute standard brain atlas space) with a voxel size of 0.5 mm using FNIRT from the FSL toolkit (<https://fsl.fmrib.ox.ac.uk/>) (Jenkinson et al., 2012). Linear registration was performed between the T1-weighted and GRE images using FLIRT, and the linear matrix and the non-linear warp field were used in a single operation to interpolate from the native GRE space to MNI space.

For all subjects, raw k-space data for the GRE acquisition was saved

for each coil and retrospectively reconstructed to generate phase and magnitude images. Individual coil phase images were processed to remove phase wraps and background phase shifts using Laplacian unwrapping (Li et al., 2014) and V-SHARP (radius = 25) (Wu et al., 2012). Per coil processed-phase maps were then combined using a GRE magnitude-weighted average to produce a single phase image. QSM maps were computed with LSQR (parameters $\text{tol}_{\text{LSQR}} = 0.01$, $\text{D2}_{\text{thres}} = 0.01$, $\text{Max_Iter} = 100$) using the STI-Suite v2.2 (Li et al., 2014). The SWI images were taken directly from the scanner console.

Six of the ten subjects were healthy elderly subjects recruited for the ASPirin in Reducing Events in the Elderly (ASPREE) clinical trial (Group, 2013) and scanned at baseline as part of the ASPREE NEURO sub-study (Ward et al., 2016b). The remaining four subjects were healthy volunteers recruited from the general population.

Manual vein tracing

A mask containing venous voxels was created for each subject by manually labelling voxels as vein or non-vein, using FSLView (Jenkinson et al., 2012), in native GRE space. The initial manual segmentation process was performed completely manually. Tracing was performed by author PW under the supervision of author NF (a clinical radiologist). The venous voxels were identified based upon SWI contrast and the authors knowledge of venous anatomy, in transverse reconstructions of the 3D SWI acquisition initially, and refined by reference to sagittal and

finally coronal reformats. Initial SWI-only masks were then overlaid side-by-side on SWI and QSM images for editing. Editing was performed slice by slice in the sagittal plane, followed by the transverse and finally the coronal plane. An example ground-truth vein segmentation is shown in Fig. 1.

Composite vein image process

The composite vein (CV) image (\ddot{X}) was constructed by combining a vein atlas, with an SWI image and a QSM image. The set of inputs (atlas, SWI and QSM) is referred to as C , where $C = \{\text{atlas, SWI, QSM}\}$. Each individual image is denoted X_c , where $c \in C$, e.g., an SWI image is referred to as X_{SWI} .

The CV method combines the three inputs with weights based on the relative predictive power of each input in different regions of the brain (Fig. 2B). The relative predictive power was captured in a *template prior* (P_c) for each of the three inputs (Fig. 2A). The inputs were normalized \dot{X}_c , and then combined using a weighted-mean with the weights derived from the priors, P_c , (Fig. 2B).

$$\ddot{X}(\vec{r}) = \frac{1}{\sum_{c=1}^C P_c(\vec{r})} \cdot \sum_{c=1}^C (P_c(\vec{r}) \cdot \dot{X}_c(\vec{r})) \quad (1)$$

The CV image, \ddot{X} , for each subject used the atlas and priors pre-calculated from the training cohort (M) (Fig. 2A). For each subject in this study, the training cohort consisted of the other nine subjects to

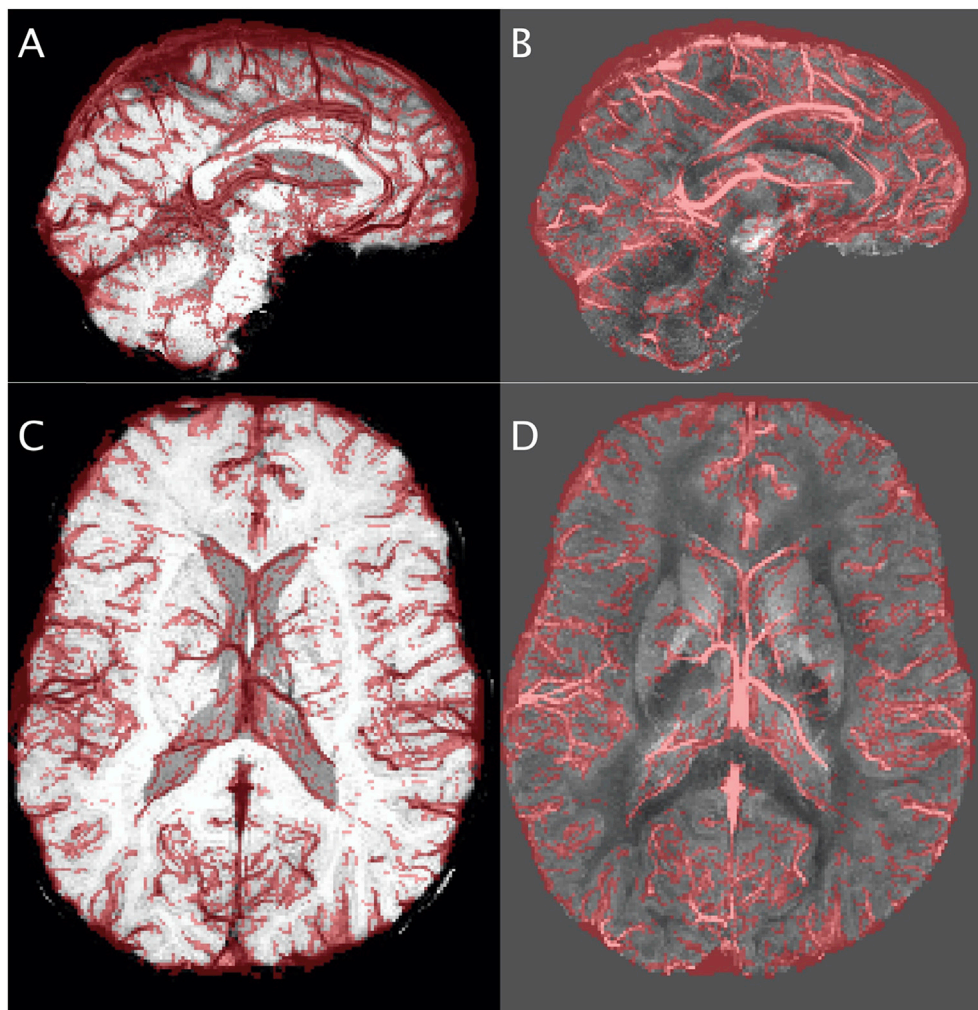


Fig. 1. Example images of the manual vein tracings. Minimum-intensity projections for SWI (A and C) and maximum-intensity projections for QSM (B and D), with a semi-transparent vein mask overlay in red. Sagittal (9 mm slab, A and B) and axial (18 mm slab, C and D) slices are shown from a single subject.

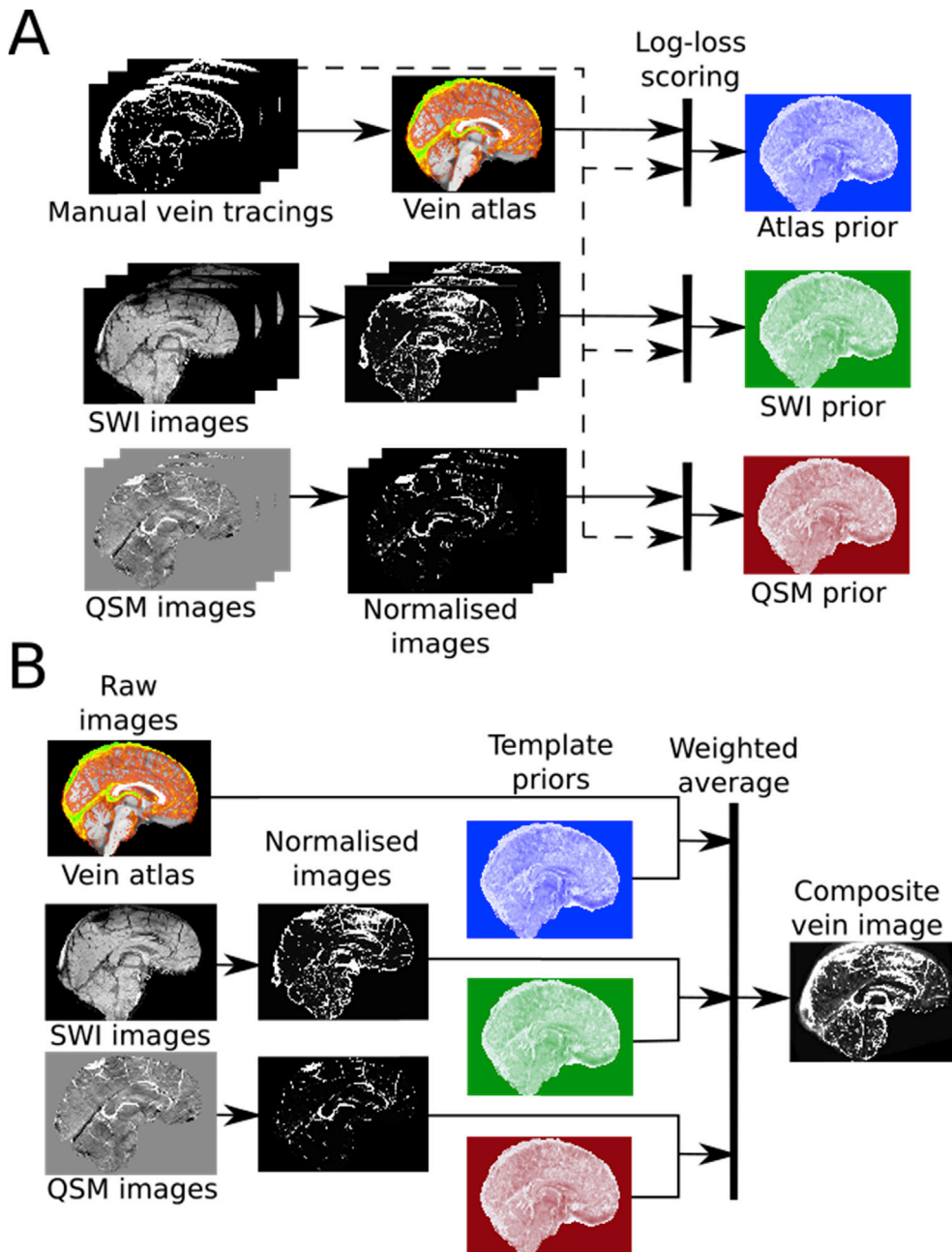


Fig. 2. Schematic describing data flow and process for training the priors and atlas (A) and producing a composite vein image (B). The training data sets (manual vein tracings, SWI images, QSM images) in (A) are used to calculate the vein atlas and template priors, and are in native space. After the log-loss scoring, the results are interpolated into MNI space to construct the template priors. The inputs (vein atlas, atlas prior, SWI prior and QSM prior) are interpolated into native space prior to the operations in (B). All operations in (B) are performed in native space. The training data set in (A) does not include the subject images in (B) to ensure independence.

ensure independence of the atlas and priors for each subject specific CV image.

In summary, the images at various stages in the processing pipeline are denoted X_c , \hat{X}_c , and \check{X} . The input images, including SWI, QSM and a vein atlas, are denoted by X_c . The normalized versions of these images are denoted \hat{X}_c , and finally after combination, the CV image is denoted \check{X} . All these images are in native GRE space. The atlas construction, normalization process, and details of the template priors are explained in the following sub-sections.

Vein atlas

Manually traced vein masks (Y) were weighted to reflect the variance and uncertainty of the human observer (W).

$$W(\vec{r}) = \begin{cases} 0.9, & Y(\vec{r}) = \text{vein} \\ 0.1, & Y(\vec{r}) \neq \text{vein} \end{cases} \quad (2)$$

The weighted tracings (W_i) for each subject, i , were interpolated into 0.5 mm MNI space and the average (mean) calculated for each voxel, \vec{r} , to construct a vein atlas.

$$X_{Atlas}(\vec{r}) = \frac{1}{|M|} \sum_{i=1}^M W_i(\vec{r}) \quad (3)$$

where M is the set of subjects in the training cohort. Visual inspection of the atlas was performed to explore the variability of vein location between subjects within the cohort. The atlas was interpolated from MNI space to native GRE space for calculating the CV image (\check{X}).

Normalization

The SWI and QSM images were processed separately to remove biases and to normalize their voxel intensities using a Gaussian mixture model (GMM) with two components (vein and non-vein). This approach has been explored previously (Ward et al., 2015, 2017b), and similar techniques have been used in blood vessel segmentation before (Bazin et al., 2016; Bériault et al., 2015, 2014; Hassouna et al., 2006).

For each image (SWI and QSM), a GMM was fit using a log-likelihood expectation-maximisation approach (Dempster et al., 1977). Both GMMs (one for SWI and one for QSM) used the same initial seed taken from the QSM images ($X_{QSM} > 0.05ppm$) to impart prior knowledge of the components.

To improve the stability and fit of the GMM to the SWI image, and mitigate any residual bias, a high-pass filter was also applied to X_{SWI} . The high-pass filtering was achieved by applying a low-pass Gaussian filter (FWHM = 10.6 voxels) to the image and subtracting this from the original image. The process was not necessary for the QSM image as the reconstruction process yields a bias-free image, and there are fewer large structures with similar voxel intensity to veins, when compared to SWI images.

The GMM process mapped the image contrasts to a unity range [0,1] and reduced the presence of subject specific biases. Normalized images (\hat{X}_{QSM} and \hat{X}_{SWI}) were produced from the mixture coefficient of the vein component for each voxel.

$$\hat{X}_{i,c} = \frac{\varpi_{c,v} Pr(V|X_{i,c}, \mu_{c,v}, \Sigma_{c,v})}{\varpi_{c,v} Pr(V|X_{i,c}, \mu_{c,v}, \Sigma_{c,v}) + \varpi_{c,\sim v} Pr(\sim V|X_{i,c}, \mu_{c,\sim v}, \Sigma_{c,\sim v})} \quad (4)$$

where c was the image (SWI or QSM), i was the voxel, and $Pr(V|X_{i,c}, \mu_{c,v}, \Sigma_{c,v})$ was the posterior probability of being labelled vein (or not vein, $\sim V$) given the distribution parameters for the image-specific GMM: μ, Σ , relative abundance ϖ , and the voxel intensity, X . Supporting information on this process has been published previously (Ward et al., 2017b; Ward, 2017f).

The QSM values were not referenced to a specific structure as any linear offset was removed by the GMM normalization. Whilst the QSM values are quantitative, the normalization procedure is still required in order to place the intensities into a common range prior to combination with the atlas and SWI values.

The atlas (X_{Atlas}) is intrinsically normalized, and was interpolated into the subject space to provide the final input (\hat{X}_{Atlas}).

Template priors

Subject specific confidence maps, $p_{i,c}$, were calculated using log-loss scoring (Dowe, 2008; Good, 1952) for each input ($c \in C$) using Eq. (5).

$$p_{i,c}(\hat{X}_{i,c}(\vec{r}), W_i(\vec{r})) = -\log(W_i(\vec{r}) \cdot (1 - \hat{X}_{i,c}(\vec{r})) + (1 - W_i(\vec{r})) \cdot \hat{X}_{i,c}(\vec{r})) \quad (5)$$

The template priors (P_c) for SWI, QSM and the vein atlas were calculated by taking the cohort mean of the confidence maps interpolated into MNI space, i.e., $p_{i,c}$ was evaluated in native space prior to averaging in MNI space to calculate P_c .

$$P_c(\vec{r}) = \frac{1}{M} \sum_{i=1}^M p_{c,i}(\hat{X}_{i,c}(\vec{r}), W_i(\vec{r})) \quad (6)$$

The predictive power represented in the priors for each information source (P_{Atlas} , P_{SWI} , and P_{QSM}) was examined visually. In order to visualize all three values, each was normalized, $\hat{P}_c(\vec{r}) = P_c(\vec{r}) / \max_d P_d(\vec{r})$, where $d \in C$, and encoded in a colour channel of a colour image (blue, green, red for P_{Atlas} , P_{SWI} , and P_{QSM} respectively).

Performance evaluation

Vein contrast in the CV image was assessed in comparison to SWI and QSM images using automated vein segmentation techniques. Three vein segmentation techniques were employed to segment the veins for each of the three image sets (the CV images, SWI images and QSM images). The first segmentation technique was a Hessian-based vesselness filter followed by an Otsu threshold (VN) (Frangi et al., 1998; Otsu, 1975). The second was a statistical method based on an Ising model Markov random field using an anisotropic graph (MRF) (Bériault et al., 2014). The third was a recursive ridge-based filter (RR) (Bazin et al., 2016). The three segmentation techniques were selected to provide a comprehensive assessment of the CV image, including a traditional and widely applied method (VN), a contemporary method designed specifically for SWI images (MRF), and a contemporary method designed specifically for QSM images (RR).

The accuracy of the vein segmentations from each image set was evaluated with standard metrics (Table 1). Many standard overlap metrics are not informative due to the high surface-to-area ratio of cerebral vein masks. To overcome this limitation, dilated versions of many of the metrics were used (Bazin et al., 2016). The metric values for the SWI and QSM image based segmentations were calculated as benchmarks, and the differences between these reference values and the segmentations computed from the CV image were examined.

Two techniques had parameters that required training (VN and MRF). A leave-one-out approach to training was taken, with the performance of the left-out subject recorded for comparison purposes. The parameters (θ) were optimized in a standardized space to minimize a composite cost function (Z), which included a regularization term (Λ).

$$Z = (1 - DSS) + \frac{MHD}{2} + \frac{AVD}{2} + \Lambda \quad (7)$$

$$\Lambda = \sqrt{\sum_i^{N_p} (\theta_i - 0.5)^2} \quad (8)$$

where N_p is the number of parameters to train. Dice similarity score (DSS) (Dice, 1945), mean Hausdorff distance (MHD) (Shonkwiler, 1989) and average volume difference (AVD) are described in Table 1. Scaling

Table 1

Vein segmentation accuracy metrics. The metrics compare the manual mask of veins (V) and non-veins (N) with an automated estimate (V' and N'). A mask morphologically dilated by one-voxel is preceded by a δ , e.g. δV is the dilated manual vein mask. Dilution was used as the boundaries of small vein may be uncertain due to bloom and partial volume. The Hausdorff distance (41), $\mathcal{D}(X, Y)$, is the mean value in a minimum distance map, i.e., the minimum distance from each surface voxel in mask X to a surface voxel in mask Y . The surface is defined as all voxels removed by a one-voxel morphological erosion.

Name	Equation
Number of true-positives (veins)	$TP = V \cap V' $, $\delta TP = \frac{1}{2}(\delta V \cap V' + V \cap \delta V')$
Number of true-negatives (non-veins)	$TN = N \cap N' $, $\delta TN = \frac{1}{2}(\delta N \cap N' + N \cap \delta N')$
Number of false-positives	$FP = N \cap V' $
Number of false-negatives	$FN = V \cap N' $
Accuracy	$ACC = \frac{\delta TP + \delta TN}{ V \cup N' }$
Sensitivity	$SE = \frac{ \delta V \cap V' }{ V' }$
Specificity	$SP = \frac{ \delta N \cap N' }{ N' }$
Positive-predictor value	$PPV = \frac{ \delta V \cap V' }{ V' }$
Negative-predictor value	$NPV = \frac{ \delta N \cap N' }{ N' }$
Dice similarity score (Dice, 1945)	$DSS = \frac{2 \cdot \delta TP}{ V' + V }$
Matthews correlation coefficient (Matthews, 1975)	$MCC = \frac{TP \cdot TN - FP \cdot FN}{\sqrt{(TP+FP)(TP+FN)(TN+FP)(TN+FN)}}$
Mean Hausdorff distance (Shonkwiler, 1989)	$MHD = \frac{1}{2}(\mathcal{D}(V, V') + \mathcal{D}(V', V))$
Average volume difference	$AVD = \frac{ FP - FN }{ V' }$

factors (division by 2 in Eq. (7)) were chosen to standardize the metric ranges as DSS is constrained to a unity range, whilst MHD and AVD are unbounded.

A gradient descent algorithm was used to search the parameter space from an initial parameter estimate. The initial parameter estimate was the optimal parameter values from a uniform random sample of the entire parameter space (1000 samples). Each iteration of the search algorithm used 32 randomly sampled potential steps. Samples were taken from a hypercube with dimensions equal to 5% of the parameter space. In all cases the cost function was found to have converged before 50 iterations. All parameters are reported in Table 2. All operations were performed in MATLAB 2015b using the MASSIVE supercomputer (Goscinski et al., 2014).

Ten sets of parameters were trained for each technique (Table 2), using a different subset of nine subjects from the ten available. The mean and standard deviation of the results are shown in Table 2. The difference in cost function value between the mean of the training set (nine subjects) and the left-out validation subject was low. In the majority of cases the validation score was better than the worst individual score in the training set.

The difference in performance was assessed between the CV images and SWI images, and CV images and QSM images. The magnitude of performance difference was quantified using Cohen's d (Cohen, 2013) and interpreted on a qualitative scale (Sawilowsky, 2009). The significance of the difference was tested using a paired two-tailed Wilcoxon signed-rank test (Wilcoxon, 1945). A description of all metrics used can be found in Table 1.

The benefit of the atlas to the CV image was examined by comparing images produced with and without the atlas. Atlas-free CV images were produced by setting the template prior for the atlas to zero.

Results

A visual inspection of a single CV image (see Fig. 3) shows the strength of combining the three inputs. The transverse slice (Fig. 3F–J) depicts the iron rich basal ganglia, which are particularly bright on QSM (Fig. 3G). The CV image is able to partially suppress the basal ganglia, whilst retaining the high vein contrast of QSM. The atlas-free CV image (Fig. 3D, I and N) does not show the same level of suppression in the basal ganglia as the CV image. The vein atlas (Fig. 3C, H and M) has been non-linearly interpolated into the subject space based on the GRE magnitude and T1 contrast. The similarity between the atlas slices, and the contrast in the SWI and QSM slices, suggests the non-linear registration can account for a large degree of inter-subject variability. The atlas shows very

Table 2
Tuned parameter descriptions for each automated segmentation technique. The trained value represents the mean and standard deviation across the 10 parameter sets trained.

Technique	Parameter	Description	Trained value		
			CV	SWI-Only	QSM-Only
MRF	β_{ratio}	Weighting factor between vein and non-vein in neighbours in clique potential calculation.	0.10±0.02	0.58±0.02	0.48±0.01
VN	α	Non-plane like factor	0.24±0.01	0.19±0.02	0.61±0.13
	β	Non-blob like factor	0.77±0.09	0.34±0.21	0.16±0.02
	γ	Intensity factor	1.61±0.08	3.89±0.22	7.65±1.23
	scale	Scales	[0.5 1.0]	[0.5 1.0]	[0.5 1.0]
RR	Recommended parameters specified by creator suitable for contrasts used (none trained).				

few veins in the basal ganglia structures (Fig. 3H) and near the dentate nuclei (Fig. 3M), which are iron rich regions where manual tracing is difficult.

All permutations of vein segmentation technique, performance metric and benchmark image (SWI or QSM) were explored, resulting in 60 comparisons. When using the CV image, 77% of the permutations showed a large or higher improvement (Cohen's d > 0.80) that was statistically significant (p < 0.05), compared to a negative effect in 5% of the permutations. The mean effect size across all permutations was 1.1 (large) and very large effects in favor of the CV image were found in 65% of comparisons. The results are shown pictographically in Fig. 4 and metric score values are reported in Table 3.

The comparisons between the atlas-free CV image and the CV image indicate the atlas contributes approximately half of the improvement observed when using the CV images, with the remaining half from combining the SWI and QSM images. The mean effect in performance metrics was a 0.5 improvement when using the atlas (Cohen's d).

The impact of the atlas is heterogeneous between the segmentation techniques. The VN and MRF methods appear to benefit strongly from the inclusion of the atlas, whilst the RR technique has almost no effect. The weakness in the RR results indicate that for the RR technique the improvement derives predominantly from the combination of the SWI and QSM contrast and not from the vein atlas.

Negative results (5%) occurred in paired-metrics and were not observed in comprehensive balanced metrics, including the DSS, MCC and MHD, which displayed performance improvements with the CV image. The scale of these quantitative improvements is varied, with the DSS improvements ranging from 0.05 to 0.39 (Table 3). Greater improvement was shown in comparison to the QSM based segmentations relative to SWI based segmentations. In paired-metrics, a corresponding positive effect was found for each negative effect in the metric pair, such as negative specificity and positive sensitivity for the QSM image when using the VN technique. In these paired cases the effect size was comparable for both positive and negative results.

Visual inspection of the segmentation results shows the MRF and VN techniques perform poorly in the basal ganglia when using QSM (Fig. 5B and F). In all examples, the CV image appears to perform equally or better than the SWI or QSM-based segmentations with fewer false-positives than SWI and fewer false-negatives than QSM. The RR segmentation technique appears less prone to false-positives in the basal ganglia, which further suggests that it benefits less from the inclusion of the atlas than the other techniques.

Inconclusive results were most common for average volume difference (AVD) (50% of comparisons, Fig. 4). AVD is a measure of the bias in the errors of the final masks, rather than a direct measure of performance. The bias can also be observed by the relative values of sensitivity (SE) and specificity (SP), or positive-predictor value (PPV) and negative-predictor value (NPV). One example of bias is application of the MRF segmentation technique to the SWI image, where AVD is poor with high SE but low SP (see Table 3). The small change in SP (0.004) must be interpreted in the context of a low number of true-positive voxels.

The similarity of vein locations between subjects was represented in the vein atlas (Fig. 6). High atlas values indicated consistent vein locations between subjects. The highest value voxels were found near the major veins, including in the superior sagittal sinus, dural sinuses, straight sinus and internal cerebral veins (green regions in Fig. 6). The deep gray matter structures, the inferior frontal and inferior temporal regions showed lower values.

The relative predictive power of the atlas, SWI and QSM template priors was observed to be heterogeneous across brain regions (Fig. 7). QSM was found to have comparatively higher power in the falx cerebri and lower power in the deep-gray matter structures, relative to SWI and the atlas. The atlas was highest in the deep-gray matter, particularly on the edge of structures. SWI had higher predictive power on the superior surface of the cortex, and lower power on the inferior surface of the brain.

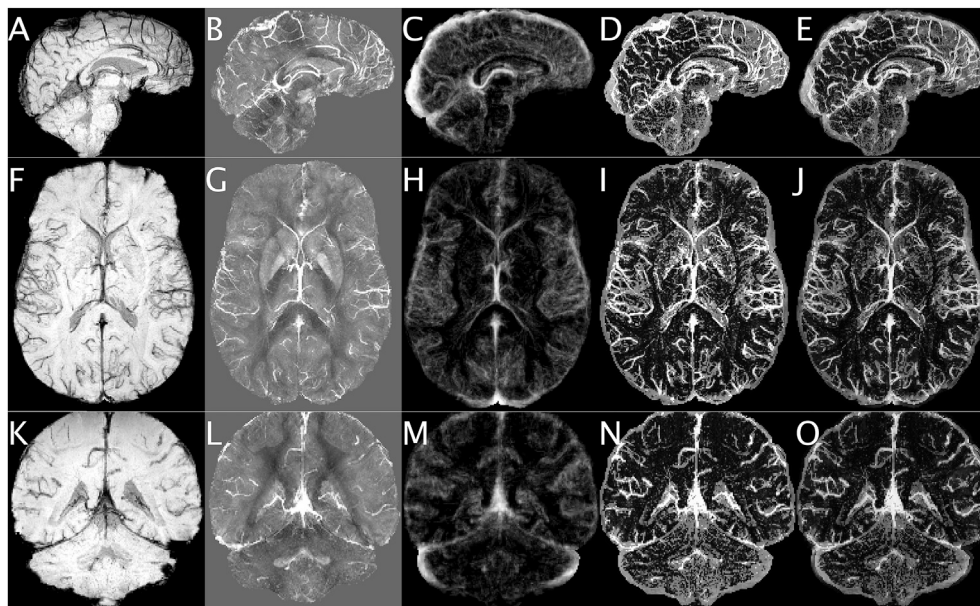


Fig. 3. Example slices of the SWI, QSM, the vein atlas, atlas-free CV images, and the CV image for a single subject. Minimum-intensity projections for SWI (A, F and K) and maximum-intensity projections for QSM, the vein atlas, the atlas-free CV image, and the CV image, are shown. Projections are all over a depth of 9 mm. Slices are taken at approximately the mid-sagittal plane in the sagittal view (A–E), through the basal ganglia in transverse view (F–J), and through the dentate nuclei in the cerebellum in the coronal view (K–O).

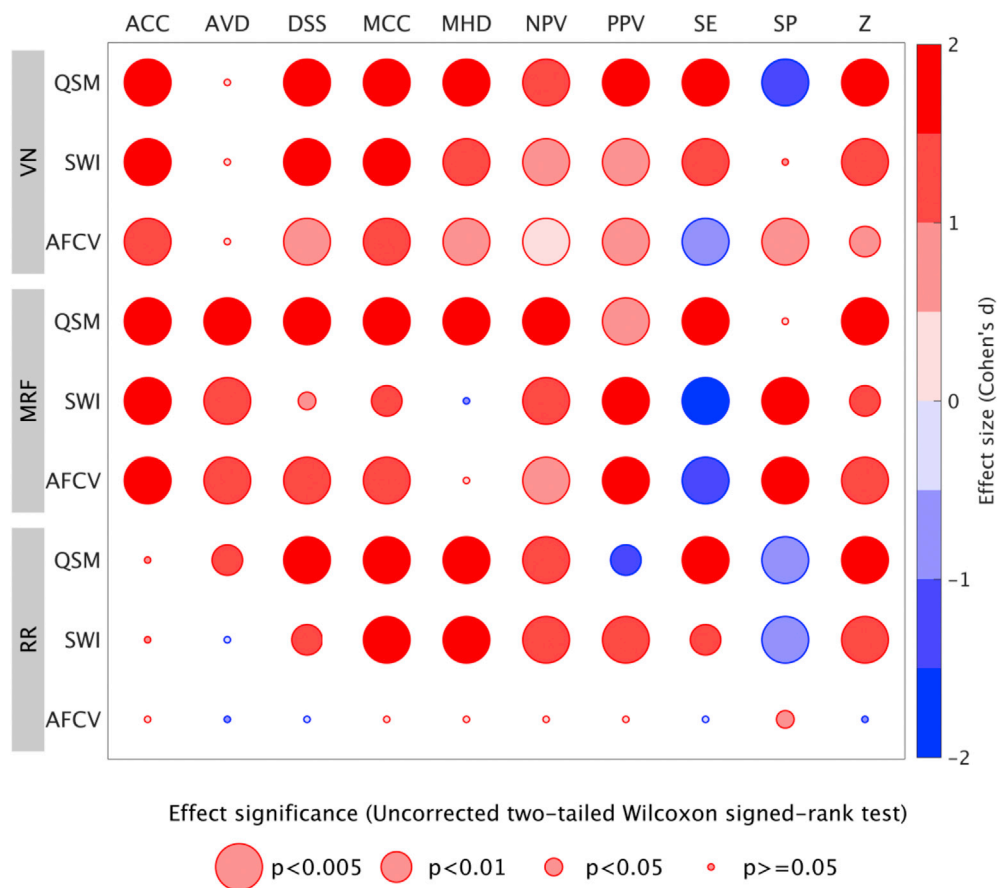


Fig. 4. The improvement in performance of three automated segmentation techniques when using the CV image compared to two alternative images. The size of the improvement (Cohen's d) and the statistical significance of the improvement (p-values) are displayed in colour and size respectively. Red circles indicate superior performance using the CV image. Large circles indicate more significant results. Each row corresponds to an automated segmentation technique (RR, MRF, or VN) and input image (SWI, QSM or atlas-free CV image (AFCV)). Each column denotes a different performance metric. All metric abbreviations are provided in Table 1. Statistical significance was measured using a two-tailed Wilcoxon signed-rank test and is uncorrected.

Table 3

Metric values (mean ± standard deviation) for all combinations of images and techniques. Accuracy (ACC), negative-predictor value (NPV) and specificity (SP) are in units of 10^{-1} to improve readability. Atlas-free CV images (AFCV) are included.

		ACC (10^{-1})	AVD	DSS	MCC	MHD	NPV (10^{-1})	PPV	SE	SP (10^{-1})
RR	CV	9.76 ± 0.0881	0.48 ± 0.32	0.66 ± 0.1	0.39 ± 0.05	1.16 ± 0.1	9.96 ± 0.0189	0.71 ± 0.1	0.69 ± 0.18	9.98 ± 0.04823
	QSM	9.71 ± 0.0375	0.86 ± 0.02	0.34 ± 0.03	0.24 ± 0.01	1.86 ± 0.13	9.93 ± 0.01781	0.88 ± 0.04	0.26 ± 0.02	10 ± 0
	SWI	9.7 ± 0.035	0.44 ± 0.12	0.51 ± 0.03	0.26 ± 0.02	1.63 ± 0.19	9.93 ± 0.01819	0.57 ± 0.08	0.48 ± 0.04	10 ± 0.00005
	AFCV	9.74 ± 0.0403	0.29 ± 0.16	0.69 ± 0.04	0.39 ± 0.02	1.17 ± 0.11	9.95 ± 0.01584	0.7 ± 0.05	0.69 ± 0.09	9.95 ± 0.03053
MRF	CV	9.77 ± 0.0286	0.28 ± 0.22	0.71 ± 0.03	0.5 ± 0.03	1.25 ± 0.16	9.97 ± 0.00876	0.72 ± 0.08	0.71 ± 0.09	9.98 ± 0.00889
	QSM	9.69 ± 0.035	0.74 ± 0.04	0.38 ± 0.04	0.25 ± 0.04	1.98 ± 0.2	9.93 ± 0.01718	0.64 ± 0.09	0.31 ± 0.03	9.98 ± 0.00718
	SWI	9.62 ± 0.0556	0.97 ± 0.4	0.66 ± 0.05	0.46 ± 0.03	1.1 ± 0.19	9.96 ± 0.01043	0.53 ± 0.06	0.92 ± 0.03	9.94 ± 0.01489
	AFCV	9.6 ± 0.065	0.94 ± 0.44	0.64 ± 0.05	0.44 ± 0.03	1.27 ± 0.18	9.96 ± 0.01036	0.54 ± 0.07	0.83 ± 0.05	9.94 ± 0.01774
VN	CV	9.82 ± 0.021	0.21 ± 0.11	0.77 ± 0.03	0.46 ± 0.03	0.98 ± 0.13	9.95 ± 0.01382	0.74 ± 0.09	0.81 ± 0.06	10 ± 0.00187
	QSM	9.55 ± 0.0578	0.25 ± 0.16	0.38 ± 0.05	0.11 ± 0.04	1.83 ± 0.15	9.92 ± 0.01929	0.32 ± 0.09	0.45 ± 0.02	10 ± 0.00069
	SWI	9.75 ± 0.0283	0.24 ± 0.14	0.67 ± 0.04	0.36 ± 0.02	1.19 ± 0.16	9.93 ± 0.01697	0.68 ± 0.09	0.69 ± 0.07	9.99 ± 0.0047
	AFCV	9.77 ± 0.0291	0.3 ± 0.27	0.73 ± 0.04	0.43 ± 0.03	1.07 ± 0.17	9.95 ± 0.01416	0.65 ± 0.08	0.85 ± 0.04	9.99 ± 0.004

Discussion

In this work, a composite vein (CV) imaging technique was proposed that combined three sources of vein information, an atlas, an SWI image, and a QSM image. The CV image showed a large improvement in vein segmentation accuracy when compared with SWI and QSM images. A robust improvement was observed in the majority of permutations across ten performance metrics and three segmentation methods.

The CV image was found to combine the complementary strengths of SWI and QSM, and produce an image with significantly improved vein

contrast by incorporating the relative predictive power of SWI and QSM in a weighted-average approach. A comprehensive analysis was performed using manually traced MRI images from ten volunteers, including anisotropic and isotropic acquisitions, multiple automated segmentation techniques, and multiple performance metrics.

The template priors characterized the anatomically heterogeneous value of the three inputs. The atlas template prior (P_{Atlas}) had higher relative values to SWI and QSM in the deep gray matter structures possibly due to non-venous iron deposits in tissue. However, the relative predictive power of SWI increased towards the center of these structures.

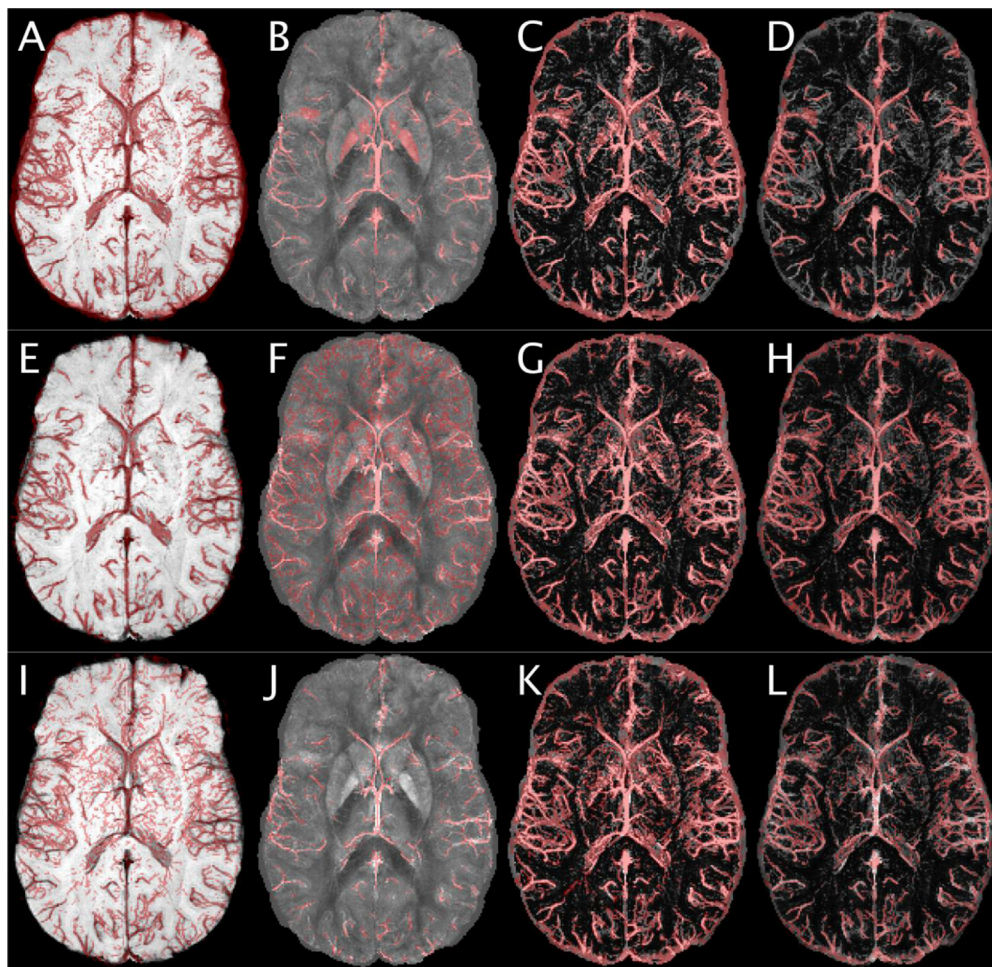


Fig. 5. Transverse projections of the segmentation output for each technique, overlaid upon the image used. The rows are for each technique: MRF (top row), VN (middle row) and RR (bottom row). The columns are for each image: SWI (left), QSM (middle-left), Atlas-Free CV (middle-right) and CV (right). Minimum-intensity projections for SWI (A, E, I) and maximum-intensity projections for QSM, Atlas-Free CV and CV image, are shown. Projections are all over a depth of 9 mm.

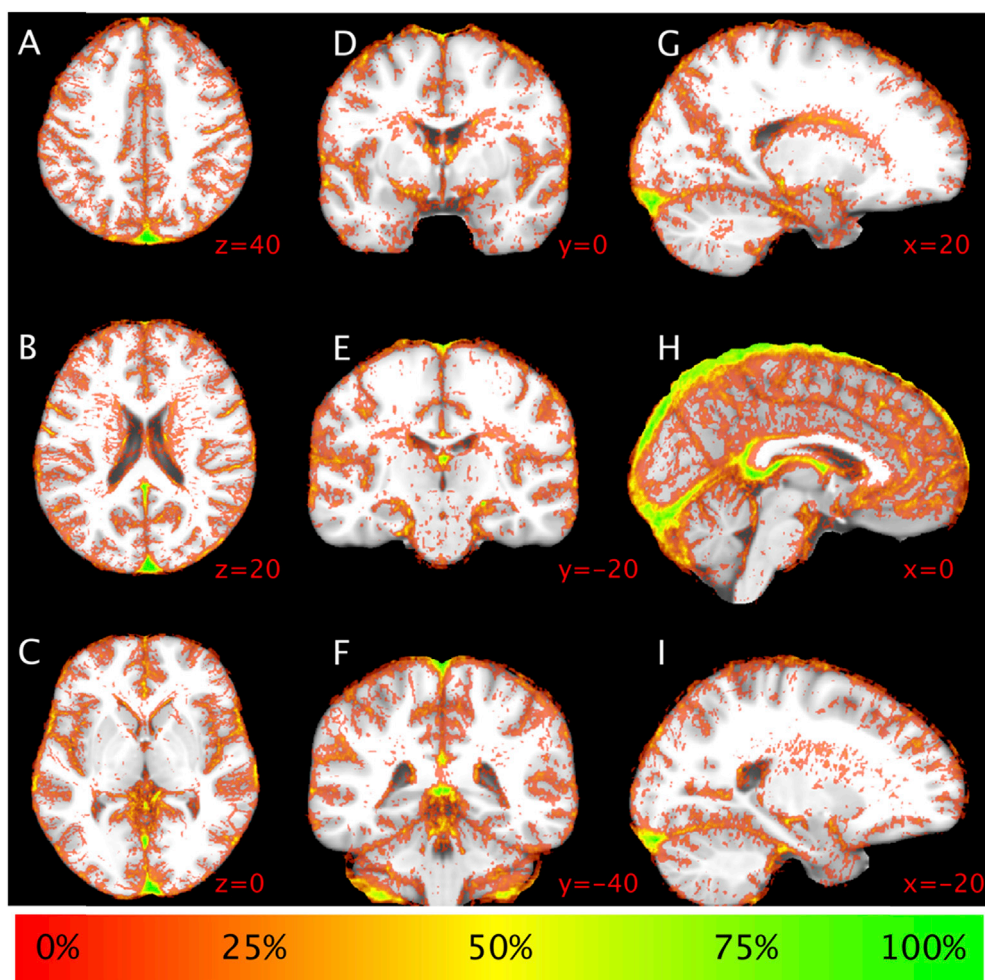


Fig. 6. Vein frequency atlas (X_{Atlas}) demonstrating high reproducibility in vein location across subjects in the major veins (e.g. sagittal sinus, green/yellow) and low reproducibility in the deep gray matter structures. Values of 0% are transparent. Slice coordinates (red) are in MNI atlas space, with axial projections (A–C), coronal projections (D–F) and sagittal projections (G–I). All slices are 0.5 mm thick.

High-pass filtering in SWI may be the cause of this effect by reducing the low-frequency spatial contrast of these iron sources and increasing the sharpness of structure boundaries. A common trend observed in the larger veins, particularly those in the interhemispheric region, was higher SWI predictive power in the center and higher QSM predictive power at the vessel wall, extending into the surrounding tissue. Extravascular enhancement on SWI images may be the source of the decrease in SWI predictive power at the vessel wall. Two exceptions to the greater predictive power of SWI in the center of larger veins were the superior sagittal sinus and the transverse sinus, where the predictive power of the atlas was higher. Decreased anatomical variability and hyper-intense GRE signal due to imperfect flow compensation are possible causes of the reduction in SWI predictive power relative to the atlas.

On the surface of the brain, neither SWI or QSM showed high predictive power away from the major sinuses (superior sagittal sinus and transverse sinuses). Accurate segmentation of veins on the brain surface is an active area of research. Success has been shown in cadavers with very high image resolution (Grabner et al., 2017), however QSM reconstruction is difficult on the surface of the brain, often leading to inferior volume coverage. Whilst SWI has coverage in this region, it also has poor contrast between veins and the skull. The template priors did not show a strong reliance upon either SWI or QSM in this area.

We can speculate on the underlying mechanisms for the heterogeneity in the template priors. SWI and QSM are derived from the same sequence, albeit in very different ways, and produce significantly different venous contrast across the brain. The contribution of the GRE

magnitude, which is orthogonal to the phase information used by both SWI and QSM, may be a key factor in the differentiation of the contrasts. Whilst magnitude provides a contrast mechanism for sub-voxel sized veins, and has been used to model partial volume in veins (McDaniel et al., 2016), it can also act as a confounder near low-signal structures. Further experiments are required to examine this directly. Greater segmentation accuracy may be acquired by combining QSM with T2* maps and separating the contributions of GRE magnitude and phase.

Approximately half of the observed improvement using the CV image could be obtained without including the vein atlas. These results suggest that the vein segmentation accuracy may be able to be improved by combining SWI and QSM alone, or by including a vein atlas in a single contrast segmentation approach. The combination of all three images provided the largest beneficial impact for segmentation accuracy.

There was minimal discrepancy between performance of the training and validation datasets. The tuned parameter values for each of the ten-independent datasets had low variance (Table 2) despite the stochastic nature of the initial parameter values. These two results indicate minimal over-fitting occurred when optimizing the technique parameters. The approach to optimization was kept consistent to ensure the findings in this study were robust, however, unique optimization for different image and technique combinations, and manual tuning, is advised when applying automated segmentation techniques. Whilst comparisons of the techniques used in this study are possible, such an assessment would be flawed without fine-tuned optimization and an intended application to focus upon.

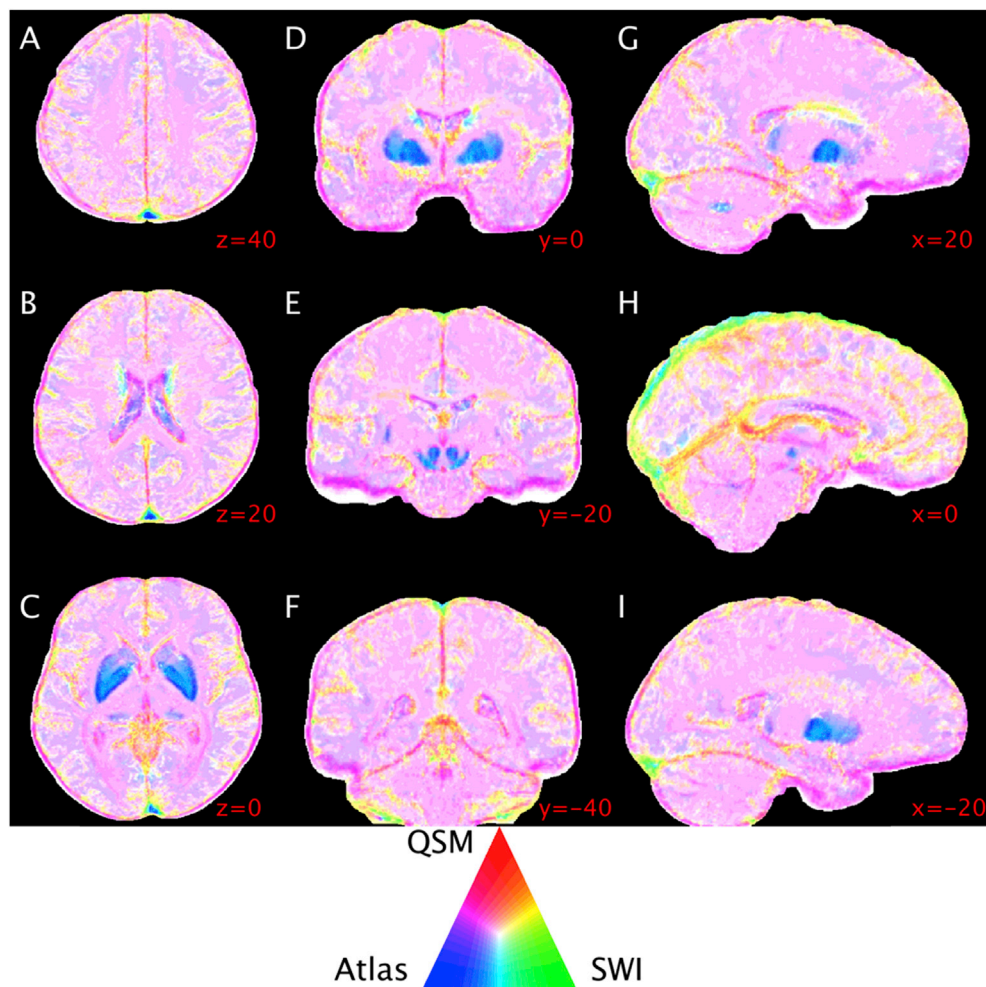


Fig. 7. Slices from the atlas, SWI and QSM template priors (P_{Atlas} , P_{SWI} , and P_{QSM} respectively), colour-coded to represent the relative weights of each. Blue regions show where P_{Atlas} is highest, green regions where P_{SWI} is highest and red regions where P_{QSM} is highest. A triangular colour-map is included. Slice coordinates (red) are in MNI atlas space, with axial projections (A–C), coronal projections (D–F) and sagittal projections (G–I). Slices are 0.5 mm in thickness.

Comparative analysis of published automated vein segmentation techniques is difficult for a number of reasons. Manually traced ground truth vein masks typically cover small manually traced regions and/or minimum-intensity projections (Bazin et al., 2016; Bériault et al., 2014; Monti et al., 2015). The small regions may not be indicative of performance across the entire brain, and are a source of variability between studies that cannot be controlled for. Studies also use different performance metrics including sensitivity and specificity (Monti et al., 2015), positive-predictor value, negative predictor value and overlap (Bazin et al., 2016), and accuracy (Bériault et al., 2014). The use of different metrics may be due to the specific application that each technique has been designed for. However, the selective use of metrics can result in one-sided conclusions being drawn, and can frustrate meta-analysis efforts.

The quantification of segmentation performance is a contentious issue (Gerig et al., 2001). To capture compensatory behavior, where one metric is optimized at the expense of another, metrics are often reported in quasi-orthogonal pairs, such as specificity and sensitivity. Although, when one label (vein) is less numerous in abundance than the other (non-vein) the trade-off between pairs will not be even due to the disparate magnitude of the denominators. Non-paired metrics, such as overlap and volume difference metrics, are more robust in these scenarios, albeit at the expense of interpretability. Comprehensive reporting of multiple metrics should be adopted to enhance both interpretability and transparency.

Both anisotropic and isotropic image acquisitions were examined in

this study. Whilst a number of published studies have shown that images acquired with anisotropic voxels are preferable for SWI images (Deistung et al., 2008; Xu and Haacke, 2006), a recently published preliminary study has shown that images acquired with isotropic voxels may be optimal for QSM reconstructions (Karsa et al., 2017). A direct comparison of anisotropic and isotropic image acquisitions was not possible in this study due to the demographic differences between the two groups of volunteers acquired with the different voxel resolutions. Future research is required to compare template priors, and segmentation accuracy, between images acquired with anisotropic and isotropic voxel sizes.

The template priors, vein atlas, and manual vein tracings are publicly available (Ward et al., 2017c). The manual vein tracing required hundreds of hours to complete, and the release of the segmented data may facilitate future work in vein segmentation techniques. The data sharing may result in a large, publicly available set of cross-validated ground truth vein images for future collaborative studies.

The value of the atlas and template priors in studies with data acquired at a higher resolution and/or higher field strength is presently unknown and requires further experimental work to be determined. Visual inspection of the vein atlas and the template priors indicates that the predictive power of the atlas is lower near smaller diameter veins, which is expected as the location of smaller veins is more varied between subjects compared to the larger veins. For this reason, the CV technique relies more heavily upon the SWI and QSM images in regions where smaller vasculature is likely to become visible at higher field. As such, we suspect the atlas and the template priors will be useful for data acquired

at higher resolution. Future work could compare the relative strengths of QSM, SWI and the CV image across different resolutions. There may also be value in calculating a multiscale atlas that captures the resolution dependent contrast of small veins.

Care is advised when applying the template priors, and the atlas, to patient cohorts. The subjects used in this study were healthy, and the findings may not hold in the presence of pathology, such as stroke or arteriovenous malformations. In general, in images that contain pathology it is necessary to perform visual inspection and careful quality control when applying automated analysis techniques and whilst using atlases.

Limitations

The findings in this study are biased by the selection of segmentation algorithms chosen for the analysis. Whilst the algorithms represent a diverse set of approaches, the CV image may not be suitable for other untested algorithms. Furthermore, both SWI and QSM are sensitive to MR sequence parameters and reconstruction techniques. The SWI images were taken directly from the MRI console to reduce any effect from in-house reconstruction, but this does not however mitigate the impact of echo time on SWI images or address the differences between MRI vendors. Studies comparing QSM reconstruction techniques have found variations in the images (Langkammer et al., 2017), and possible echo time dependencies (Sood et al., 2017). The GMM stability and the template priors may not be optimal for data acquired with different parameters or processed using different algorithms.

A distinction should be considered between accurate vein segmentation and accurate imitation of manually traced vein masks. The tracings are not a direct measure of veins, but a subjective radiological interpretation (Drew et al., 2013), and are produced in the presence of the artefacts that occur in susceptibility-based MRI. A ground truth that is independent of MRI-based artefacts would be required to directly quantify vein segmentation accuracy.

Furthermore, only binary masks have been addressed in this work. However, vein geometry does not conform to a cubic grid. Recent work has found significant error associated with binary representations of veins in simulated QSM images (Ward et al., 2017e). Further work will explore non-binary manual tracings to incorporate both partial volume and marker uncertainty.

Conclusions

A large improvement in vein segmentation accuracy was achieved using the composite vein image technique. The composite vein image technique incorporates the heterogeneous vein contrast profile across the brain to extract the complementary information available from SWI and QSM images, and a vein atlas. The technique's performance was evaluated with multiple segmentation techniques and metrics. The accuracy provided by the composite vein image allows improved quantification of cerebrovenous topology and cerebrovascular oxygenation using MRI.

Acknowledgements

We thank the investigators of the ASPREE study and the ASPREE-NEURO sub-study for the coordination and recruitment of the volunteers. We thank the volunteers for their time and willingness to participate.

The Alzheimer's Australia Dementia Research Foundation (AADRF) the Victorian Life Sciences Computation Initiative (VLSCI), the Multi-model Australian Sciences Imaging and Visualisation Environment (MASSIVE) and the National Health and Medical Research Council (NHMRC) supported this work (NHMRC Grant APP1086188).

We would like to thank Dr. Pierre-Louis Bazin and Dr. Silvain Bériault for their assistance in implementing and applying their vein segmentation methods.

Initial work and preliminary findings related to this study were previously presented at annual meetings of the International Society for Magnetic Resonance in Medicine (Ward et al., 2015, 2016a, 2017d).

References

- Bazin, P.L., Plessis, V., Fan, A.P., Villringer, A., Gauthier, C.J., 2016. Vessel segmentation from quantitative susceptibility maps for local oxygenation venography. In: 2016 IEEE 13th International Symposium on Biomedical Imaging (ISBI), pp. 1135–1138. <https://doi.org/10.1109/ISBI.2016.7493466>. Presented at the 2016 IEEE 13th International Symposium on Biomedical Imaging (ISBI).
- Bériault, S., Archambault-Wallenburg, M., Sadikot, A., Louis Collins, D., Bruce Pike, G., 2014. Automatic markov random field segmentation of susceptibility-weighted MR venography. In: *Clinical Image-based Procedures. Translational Research in Medical Imaging*, pp. 39–47. *Lecture Notes in Computer Science*.
- Bériault, S., Xiao, Y., Collins, D.L., Pike, G.B., 2015. Automatic SWI venography segmentation using conditional random fields. *IEEE Trans. Med. Imaging* 34, 2478–2491. <https://doi.org/10.1109/TMI.2015.2442236>.
- Betts, M.J., Acosta-Cabronero, J., Cardenas-Blanco, A., Nestor, P.J., Düzel, E., 2016. High-resolution characterisation of the aging brain using simultaneous quantitative susceptibility mapping (QSM) and R2* measurements at 7T. *NeuroImage* 138, 43–63. <https://doi.org/10.1016/j.neuroimage.2016.05.024>.
- Cohen, J., 2013. *Statistical Power Analysis for the Behavioral Sciences*. Routledge.
- Deistung, A., Rauscher, A., Sedlacik, J., Stadler, J., Witoszynskij, S., Reichenbach, J.R., 2008. Susceptibility weighted imaging at ultra high magnetic field strengths: theoretical considerations and experimental results. *Magn. Reson. Med.* 60, 1155–1168. <https://doi.org/10.1002/mrm.21754>.
- Deistung, A., Schweser, F., Reichenbach, J.R., 2016. Overview of quantitative susceptibility mapping. *NMR Biomed.* <https://doi.org/10.1002/nbm.3569> n/a-n/a.
- Deistung, A., Schweser, F., Reichenbach, J.R., 2013. Optimal enhancement of brain structures by combining different MR contrasts: demonstration of venous vessel enhancement in multi-echo gradient-echo MRI. In: *Proceedings of the 21st Annual Meeting of the International Society for Magnetic Resonance in Medicine*, p. 695. Presented at the ISMRM.
- Dempster, A.P., Laird, N.M., Rubin, D.B., 1977. Maximum likelihood from incomplete data via the EM algorithm. *J. R. Stat. Soc. Ser. B Methodol.* 39, 1–38.
- Dice, L.R., 1945. Measures of the amount of ecologic association between species. *Ecology* 26, 297–302. <https://doi.org/10.2307/1932409>.
- Dowe, D.L., 2008. Foreword re C. S. Wallace. *Comput. J.* 51, 523–560. <https://doi.org/10.1093/comjnl/bxm117>.
- Drew, T., Vo, M.L.H., Wolfe, J.M., 2013. The invisible gorilla strikes again: sustained inattention blindness in expert observers. *Psychol. Sci.* 24, 1848–1853. <https://doi.org/10.1177/0956797613479386>.
- Fan, A.P., Bilgic, B., Gagnon, L., Witzel, T., Bhat, H., Rosen, B.R., Adalsteinsson, E., 2014. Quantitative oxygenation venography from MRI phase. *Magn. Reson. Med.* 72, 149–159. <https://doi.org/10.1002/mrm.24918>.
- Fan, A.P., Govindarajan, S.T., Kinkel, R.P., Madigan, N.K., Nielsen, A.S., Benner, T., Tinelli, E., Rosen, B.R., Adalsteinsson, E., Mainero, C., 2015. Quantitative oxygen extraction fraction from 7-Tesla MRI phase: reproducibility and application in multiple sclerosis. *J. Cereb. Blood Flow. Metab.* 35, 131–139. <https://doi.org/10.1038/jcbfm.2014.187>.
- Frangi, A.F., Niessen, W.J., Vincken, K.L., Viergever, M.A., 1998. Multiscale vessel enhancement filtering. In: Wells, W.M., Colchester, A., Delp, S. (Eds.), *Medical Image Computing and Computer-assisted Intervention — MICCAI'98, Lecture Notes in Computer Science*. Springer Berlin Heidelberg, pp. 130–137. <https://doi.org/10.1007/BFb0056195>.
- Fujima, N., Kudo, K., Terae, S., Ishizaka, K., Yazu, R., Zaitus, Y., Tha, K.K., Yoshida, D., Tsukahara, A., Haacke, M.E., Sasaki, M., Shirato, H., 2011. Non-invasive measurement of oxygen saturation in the spinal vein using SWI: quantitative evaluation under conditions of physiological and caffeine load. *NeuroImage* 54, 344–349. <https://doi.org/10.1016/j.neuroimage.2010.08.020>.
- Gerig, G., Jomier, M., Chakos, M., 2001. Valmet: a new validation tool for assessing and improving 3D object segmentation. In: Niessen, W.J., Viergever, M.A. (Eds.), *Medical Image Computing and Computer-assisted Intervention – MICCAI 2001, Lecture Notes in Computer Science*. Springer Berlin Heidelberg, pp. 516–523. https://doi.org/10.1007/3-540-45468-3_62.
- Good, I.J., 1952. Rational decisions. *J. R. Stat. Soc. Ser. B Methodol.* 14, 107–114.
- Goodwin, J.A., Kudo, K., Shinohe, Y., Higuchi, S., Uwano, I., Yamashita, F., Sasaki, M., 2015. Susceptibility-weighted phase imaging and oxygen extraction fraction measurement during sedation and sedation recovery using 7T MRI. *J. Neuroimaging* 25, 575–581. <https://doi.org/10.1111/jon.12192>.
- Goscinski, W.J., McIntosh, P., Felzmann, U.C., Maksimenko, A., Hall, C.J., Gureyev, T., Thompson, D., Janke, A., Galloway, G., Killeen, N.E.B., Raniga, P., Kaluza, O., Ng, A., Poudel, G., Barnes, D., Nguyen, T., Bonnington, P., Egan, G.F., 2014. The multi-modal Australian Sciences Imaging and Visualization Environment (MASSIVE) high performance computing infrastructure: applications in neuroscience and neuroinformatics research. *Front. Neuroinformatics* 8, 30. <https://doi.org/10.3389/fninf.2014.00030>.
- Grabner, G., Dal-Bianco, A., Hametner, S., Lassmann, H., Trattnig, S., 2014. Group specific vein-atlasing: an application for analyzing the venous system under normal and multiple sclerosis conditions. *J. Magn. Reson. Imaging* 40, 655–661. <https://doi.org/10.1002/jmri.24393>.
- Grabner, G., Haider, T., Glassner, M., Rauscher, A., Traxler, H., Trattnig, S., Robinson, S.D., 2017. Post mortem validation of MRI-identified veins on the surface

- of the cerebral cortex as potential landmarks for neurosurgery. *Front. Neurosci.* 11 <https://doi.org/10.3389/fnins.2017.00355>.
- Group, A.I., 2013. Study design of Aspirin in Reducing Events in the Elderly (ASPREE): a randomized, controlled trial. *Contemp. Clin. Trials* 36, 555–564. <https://doi.org/10.1016/j.cct.2013.09.014>.
- Haacke, E.M., Cheng, Y.-C.N., Reichenbach, J.R., 2004. Susceptibility weighted imaging (SWI). *Magn. Reson. Med.* 52, 612–618. <https://doi.org/10.1002/mrm.20198>.
- Hassouna, M.S., Farag, A.A., Hushek, S., Moriarty, T., 2006. Cerebrovascular segmentation from TOF using stochastic models. *Med. Image Anal.* 10, 2–18. <https://doi.org/10.1016/j.media.2004.11.009>.
- Hsu, C.-Y., Schneller, B., Alaraj, A., Flannery, M., Zhou, X.J., Linninger, A., 2017. Automatic recognition of subject-specific cerebrovascular trees. *Magn. Reson. Med.* 77, 398–410. <https://doi.org/10.1002/mrm.26087>.
- Jain, V., Langham, M.C., Wehrli, F.W., 2010. MRI estimation of global brain oxygen consumption rate. *J. Cereb. Blood Flow. Metab.* 30, 1598–1607. <https://doi.org/10.1038/jcbfm.2010.49>.
- Jenkinson, M., Beckmann, C.F., Behrens, T.E.J., Woolrich, M.W., Smith, S.M., 2012. FSL. *NeuroImage*. 20 YEARS fMRI 62, 782–790. <https://doi.org/10.1016/j.neuroimage.2011.09.015>.
- Karsa, A., Punwani, S., Shmueli, K., 2017. Resolution and coverage for accurate susceptibility maps: comparing brain images with simulations. In: *Proceedings of the 25th Annual Meeting of the International Society for Magnetic Resonance in Medicine*, p. 3677. Presented at the ISMRM, Honolulu, USA.
- Kociński, M., Materka, A., Deistung, A., Reichenbach, J., Lundervold, A., 2017. Towards multi-scale personalized modeling of brain vasculature based on magnetic resonance image processing. In: *2017 International Conference on Systems, Signals and Image Processing (IWSSIP)*, pp. 1–5. <https://doi.org/10.1109/IWSSIP.2017.7965604>. Presented at the 2017 International Conference on Systems, Signals and Image Processing (IWSSIP).
- Langkammer, C., Schweser, F., Shmueli, K., Kames, C., Li, X., Guo, L., Milovic, C., Kim, J., Wei, H., Bredies, K., Buch, S., Guo, Y., Liu, Z., Meineke, J., Rauscher, A., Marques, J.P., Bilgic, B., 2017. Quantitative susceptibility mapping: report from the 2016 reconstruction challenge. *Magn. Reson. Med.* <https://doi.org/10.1002/mrm.26830>.
- Lesage, D., Angelini, E.D., Bloch, I., Funke-Lea, G., 2009. A review of 3D vessel lumen segmentation techniques: models, features and extraction schemes. *Med. Image Anal.* Incl. Special Sect. Comput. Biomechanics Med. 13, 819–845. <https://doi.org/10.1016/j.media.2009.07.011>.
- Li, M., Hu, J., Miao, Y., Shen, H., Tao, D., Yang, Z., Li, Q., Xuan, S.Y., Raza, W., Alzubaidi, S., Haacke, E.M., 2013. In Vivo measurement of oxygenation changes after stroke using susceptibility weighted imaging filtered phase data. *Plos One* 8, e63013. <https://doi.org/10.1371/journal.pone.0063013>.
- Li, W., Avram, A.V., Wu, B., Xiao, X., Liu, C., 2014. Integrated Laplacian-based phase unwrapping and background phase removal for quantitative susceptibility mapping. *NMR Biomed.* 27, 219–227. <https://doi.org/10.1002/nbm.3056>.
- Li, W., Wang, N., Yu, F., Han, H., Cao, W., Romero, R., Tantiwongkosi, B., Duong, T.Q., Liu, C., 2015. A method for estimating and removing streaking artifacts in quantitative susceptibility mapping. *NeuroImage* 108, 111–122. <https://doi.org/10.1016/j.neuroimage.2014.12.043>.
- Liu, Z., Kee, Y., Zhou, D., Wang, Y., Spincemaille, P., 2017. Preconditioned total field inversion (TFI) method for quantitative susceptibility mapping. *Magn. Reson. Med.* 78, 303–315. <https://doi.org/10.1002/mrm.26331>.
- Liu, Z., Li, Y., 2016. Cortical cerebral blood flow, oxygen extraction fraction, and metabolic rate in patients with middle cerebral artery stenosis or acute stroke. *Am. J. Neuroradiol.* 37, 607–614. <https://doi.org/10.3174/ajnr.A4624>.
- Manniesing, R., Viergever, M.A., Niessen, W.J., 2006. Vessel enhancing diffusion: a scale space representation of vessel structures. *Med. Image Anal.* 10, 815–825. <https://doi.org/10.1016/j.media.2006.06.003>.
- Marques, J.P., Bowtell, R., 2005. Application of a Fourier-based method for rapid calculation of field inhomogeneity due to spatial variation of magnetic susceptibility. *Concepts Magn. Reson. Part B Magn. Reson. Eng.* 25B, 65–78. <https://doi.org/10.1002/cmr.b.20034>.
- Matthews, B.W., 1975. Matthews, B.: comparison of the predicted and observed secondary structure of T4 phage lysozyme. *Biochim. Biophys. Acta Protein Struct.* 405 (2), 442–451. [https://doi.org/10.1016/0005-2795\(75\)90109-9](https://doi.org/10.1016/0005-2795(75)90109-9).
- McDaniel, P., Bilgic, B., Fan, A.P., Stout, J.N., Adalsteinsson, E., 2016. Mitigation of partial volume effects in susceptibility-based oxygenation measurements by joint utilization of magnitude and phase (JUMP). *Magn. Reson. Med.* <https://doi.org/10.1002/mrm.26227>.
- Monti, S., Palma, G., Borrelli, P., Tedeschi, E., Coccozza, S., Salvatore, M., Mancini, M., 2015. A multiparametric and multiscale approach to automated segmentation of brain veins. In: *2015 37th Annual International Conference of the IEEE Engineering in Medicine and Biology Society (EMBC)*, pp. 3041–3044. <https://doi.org/10.1109/EMBC.2015.7319033>. Presented at the 2015 37th Annual International Conference of the IEEE Engineering in Medicine and Biology Society (EMBC).
- Otsu, N., 1975. A threshold selection method from gray-level histograms. *Automatica* 11, 23–27.
- Pauling, L., Coryell, C.D., 1936. The magnetic properties and structure of hemoglobin, oxyhemoglobin and carbonmonoxyhemoglobin. *Proc. Natl. Acad. Sci.* 22, 210–216. <https://doi.org/10.1073/pnas.22.4.210>.
- Rodgers, Z.B., Detre, J.A., Wehrli, F.W., 2016. MRI-based methods for quantification of the cerebral metabolic rate of oxygen. *J. Cereb. Blood Flow. Metab.* 36, 1165–1185. <https://doi.org/10.1177/0271678X16643090>.
- Rodgers, Z.B., Jain, V., Englund, E.K., Langham, M.C., Wehrli, F.W., 2013. High temporal resolution MRI quantification of global cerebral metabolic rate of oxygen consumption in response to apneic challenge. *J. Cereb. Blood Flow. Metab.* 33, 1514–1522. <https://doi.org/10.1038/jcbfm.2013.110>.
- Salomir, R., de Senneville, B.D., Moonen, C.T., 2003. A fast calculation method for magnetic field inhomogeneity due to an arbitrary distribution of bulk susceptibility. *Concepts Magn. Reson. Part B Magn. Reson. Eng.* 19B, 26–34. <https://doi.org/10.1002/cmr.b.10083>.
- Santhosh, K., Kesavadas, C., Thomas, B., Gupta, A.K., Thamburaj, K., Kapilamoorthy, T.R., 2009. Susceptibility weighted imaging: a new tool in magnetic resonance imaging of stroke. *Clin. Radiol.* 64, 74–83. <https://doi.org/10.1016/j.crad.2008.04.022>.
- Sawilowsky, S., 2009. *New Effect Size Rules of Thumb (Theor. Behav. Found. Educ. Fac. Publ.)*.
- Shonkwiler, R., 1989. An image algorithm for computing the Hausdorff distance efficiently in linear time. *Inf. Process. Lett.* 30, 87–89. [https://doi.org/10.1016/0020-0190\(89\)90114-2](https://doi.org/10.1016/0020-0190(89)90114-2).
- Sood, S., Urriola, J., Reutens, D., O'Brien, K., Bollmann, S., Barth, M., Vegh, V., 2017. Echo time-dependent quantitative susceptibility mapping contains information on tissue properties. *Magn. Reson. Med.* 77, 1946–1958. <https://doi.org/10.1002/mrm.26281>.
- Vigneau-Roy, N., Bernier, M., Descoteaux, M., Whittingstall, K., 2014. Regional variations in vascular density correlate with resting-state and task-evoked blood oxygen level-dependent signal amplitude. *Hum. Brain Mapp.* 35, 1906–1920. <https://doi.org/10.1002/hbm.22301>.
- Wang, Y., Liu, T., 2015. Quantitative susceptibility mapping (QSM): decoding MRI data for a tissue magnetic biomarker. *Magn. Reson. Med.* 73, 82–101. <https://doi.org/10.1002/mrm.25358>.
- Ward, P.G.D., Ferris, N.J., Ng, A.C.L., Barnes, D.G., Dowe, D.L., Egan, G.F., Raniga, P., 2015. Venous segmentation using Gaussian mixture models and Markov random fields. In: *Proceedings of the 23rd Annual Meeting of the International Society for Magnetic Resonance in Medicine*, p. 3759. <https://doi.org/10.13140/RG.2.2.16479.87202>. Presented at the ISMRM, Toronto, Canada.
- Ward, P.G.D., 2017a. Composite Vein Imaging for Susceptibility-based Magnetic Resonance Imaging [WWW Document]. <https://github.com/philgd/CVI-MRI>.
- Ward, P.G.D., Ferris, N.J., Raniga, P., Ng, A.C.L., Barnes, D.G., Dowe, D.L., Egan, G.F., 2017b. Vein segmentation using shape-based Markov random fields. In: *Proceedings of the 14th IEEE International Symposium on Biomedical Imaging: from Nano to Macro*. Presented at the 14th IEEE International Symposium on Biomedical Imaging (ISBI). IEEE, Melbourne, Australia, pp. 1133–1136. <https://doi.org/10.1109/ISBI.2017.7950716>.
- Ward, P.G.D., Ferris, N.J., Raniga, P., Ng, A.C.L., Dowe, D.L., Barnes, D., Egan, G.F., 2017c. Combined magnetic susceptibility contrast for vein segmentation from a single MRI acquisition using a vein frequency atlas. *Figshare*. <https://doi.org/10.4225/03/57B6AB25DDBDC>.
- Ward, P.G.D., Ferris, N.J., Raniga, P., Ng, A.C.L., Dowe, D.L., Barnes, D.G., Egan, G.F., 2017d. Regional variations in cerebral venous contrast using susceptibility-based MRI. In: *Proceedings of the 25th Annual Meeting of the International Society for Magnetic Resonance in Medicine*, p. 1450. Presented at the ISMRM, Honolulu, USA.
- Ward, P.G.D., Fan, A.P., Raniga, P., Barnes, D.G., Dowe, D.L., Ng, A.C.L., Egan, G.F., 2017e. Improved quantification of cerebral vein oxygenation using partial volume correction. *Front. Neurosci.* 11 <https://doi.org/10.3389/fnins.2017.00089>.
- Ward, P.G.D., 2017f. *Automated Characterization of Cerebral Veins (PhD Thesis)*. Monash University, Clayton, Australia. <https://doi.org/10.4225/03/58d09aaa98b87>.
- Ward, P.G.D., Raniga, P., Ferris, N.J., Ng, A.C.L., Barnes, D.G., Dowe, D.L., Storey, E., Woods, R.L., Egan, G.F., 2016a. Venous metrics in a large cohort of healthy elderly individuals from susceptibility-weighted images and quantitative susceptibility maps. In: *Proceedings of the 24th Annual Meeting of the International Society for Magnetic Resonance in Medicine*. Singapore, p. 3795. <https://doi.org/10.13140/RG.2.2.19835.31529>.
- Ward, S.A., Raniga, P., Ferris, N.J., Woods, R.L., Storey, E., Bailey, M.J., Brodtmann, A., Yates, P.A., Donnan, G.A., Trevaks, R.E., Wolfe, R., Egan, G.F., McNeil, J.J., Authorship, Joint Senior, Group, on behalf of the A. investigator, 2016b. ASPREE-NEURO study protocol: a randomized controlled trial to determine the effect of low-dose aspirin on cerebral microbleeds, white matter hyperintensities, cognition, and stroke in the healthy elderly. *Int. J. Stroke*. <https://doi.org/10.1177/1747493016669848>.
- Wharton, S., Schäfer, A., Bowtell, R., 2010. Susceptibility mapping in the human brain using threshold-based k-space division. *Magn. Reson. Med.* 63, 1292–1304. <https://doi.org/10.1002/mrm.22334>.
- Wilcoxon, F., 1945. Individual comparisons by ranking methods. *Biom. Bull.* 1, 80–83.
- Wu, B., Li, W., Guidon, A., Liu, C., 2012. Whole brain susceptibility mapping using compressed sensing. *Magn. Reson. Med.* 67, 137–147. <https://doi.org/10.1002/mrm.23000>.
- Xu, Y., Haacke, E.M., 2006. The role of voxel aspect ratio in determining apparent vascular phase behavior in susceptibility weighted imaging. *Magn. Reson. Imaging* 24, 155–160. <https://doi.org/10.1016/j.mri.2005.10.030>.